

1 **Upper mantle slab under Alaska: contribution to anomalous**  
2 **core-phase observations on south-Sandwich to Alaska paths**

3

4 **Authors:** Daniel A. Frost<sup>1\*</sup>, Barbara Romanowicz<sup>1,2,3</sup>, Steve Roecker<sup>4</sup>

5

6 **Affiliations:**

7 <sup>1</sup>Earth & Planetary Science, University of California, Berkeley, CA, USA

8 <sup>2</sup>Institut de Physique du Globe de Paris, Paris, France

9 <sup>3</sup>College de France, Paris, France

10 <sup>4</sup>Rensselaer Polytechnic Institute, Troy, NY, USA

11

12 \*Correspondence to: [dafrost@berkeley.edu](mailto:dafrost@berkeley.edu)

13

14 **Abstract**

15 Observations of travel time anomalies of inner core-sensitive PKPdf  
16 seismic body waves, as a function of path orientation with respect to  
17 the earth's rotation axis, have been interpreted as evidence of  
18 anisotropy in the inner core. Paths from earthquakes in the South  
19 Sandwich Islands to stations in Alaska show strongly anomalous travel  
20 times, with a large spread that is not compatible with simple models of  
21 anisotropy. Here we assess the impact of strong velocity heterogeneity  
22 under Alaska on the travel times, directions of arrival and amplitudes  
23 of PKPdf. We use 3D ray-tracing and 2.5D waveform modelling through

24 a new, high-resolution tomography model of the upper mantle beneath  
25 Alaska. We find that the structure beneath Alaska, notably the  
26 subducting slab, is reflected in the patterns of these PKPdf  
27 observations, and this can be replicated by our model. We also find  
28 similar patterns in observed teleseismic P waves that can likewise be  
29 explained by our slab model. We conclude that at least 2 s of the travel  
30 time anomaly often attributed to inner core anisotropy is due to slab  
31 effects in the upper mantle beneath Alaska.

32

### 33 **Introduction**

34 The observation of directionally dependent travel time anomalies of  
35 inner-core sensitive body waves, combined with anomalous splitting of  
36 core-sensitive normal modes, have been interpreted as evidence of  
37 cylindrical velocity anisotropy within the inner core (IC) (Morelli et al.,  
38 1986; Woodhouse et al., 1986). The fast axis of anisotropy is within  
39 several degrees of the rotation axis, while the slow direction migrates  
40 from in the plane of the equator to within  $55^\circ$  of the rotation axis with  
41 increasing depth in the IC (e.g. Ishii and Dziewonski, 2002; Lythgoe *et*  
42 *al.*, 2014; Frost and Romanowicz, 2019). This anisotropy has been  
43 interpreted as resulting from preferred alignment of anisotropic iron  
44 crystals within the inner core (Stixrude and Cohen, 1995). The  
45 magnitude of anisotropy has been shown to vary between 0 and 8%,  
46 dependent on depth of sampling (e.g. Vinnik et al., 1994; Lythgoe *et*

47 *al.*, 2014). Meanwhile, its dependence on the longitude of sampling has  
48 been interpreted as evidence of a hemispherical dichotomy, where the  
49 quasi-western hemisphere shows stronger anisotropy of around 4% in  
50 most models, while the quasi-eastern hemisphere show weaker  
51 anisotropy of 1-2% (Creager, 1999; Irving and Deuss, 2011; Tanaka  
52 and Hamaguchi, 1997)

53

54 Inner core anisotropy is investigated using the core-sensitive body  
55 wave, PKP, which comprises two branches sensitive only to the outer  
56 core, PKPbc and PKPab, and one branch sensitive to both the outer and  
57 inner cores, PKPdf. The PKPab and PKPbc branches are often used as  
58 references, in order to reduce the influence of source and origin time  
59 errors, as well as upper mantle velocity heterogeneity, on the recorded  
60 differential travel times. Residual travel times of PKPdf relative to a 1D  
61 reference model show a dependence on the angle of the inner core  
62 portion of the ray relative to the rotation axis,  $\xi$  (Morelli et al., 1986).  
63 Rays with  $\xi < 35^\circ$  are referred to as polar and are roughly aligned with  
64 the fast axis of anisotropy. These rays show negative PKPdf travel time  
65 anomalies of up to 10 seconds (Morelli, Dziewonski and Woodhouse,  
66 1986; Shearer, 1994; Su and Dziewonski, 1995; Li and Cormier, 2002;  
67 Cao and Romanowicz, 2007; Lythgoe *et al.*, 2014; Romanowicz *et al.*,  
68 2015, Frost et al., *in revision*). Here, we use observed PKPdf travel

69 times measured relative to predictions from a 1D reference model,  
70 referred to as absolute PKPdf travel time anomalies.

71

72 Resolution of the global pattern of inner core anisotropy is limited by  
73 spatially heterogeneous sampling of the IC on polar paths. Previous  
74 studies have noted the strongly anomalous character of travel times  
75 on polar paths from sources in the South Sandwich Islands (SSI) to  
76 stations Alaska, where rays with a range in  $\xi$  of only  $6^\circ$  ( $26 < \xi < 32^\circ$ )  
77 show a range of 6 s in travel time anomaly, in contrast with  $\sim 3$  s for  
78 the global data in the same  $\xi$  range, (Romanowicz et al., 2003; Garcia  
79 et al., 2006; Leykam et al., 2010; Tkalčić, 2010; Tkalčić *et al.*, 2015;  
80 Frost and Romanowicz, 2017). This behaviour is seen for both PKPdf  
81 absolute and PKPbc-df and PKPab-df relative travel times  
82 (Supplementary Figure 1). This SSI-Alaska path may also show  
83 variations in the amplitude of PKPdf (Long et al., 2018). The SSI-Alaska  
84 anomaly has led to complications in the interpretation of inner core  
85 structure (Tkalčić, 2010).

86

87 Notably, given the frequent seismicity in the SSI, data from this source  
88 region to stations in Alaska are often over-represented in catalogues of  
89 IC travel time anomalies (e.g. Tkalčić et al., 2002). Previous studies  
90 have attempted to explain the discrepant SSI-Alaska PKP data by  
91 invoking regional variations in the strength of IC anisotropy (Tkalčić,

92 2010). Other studies have argued for a source outside of the IC,  
93 specifically velocity anomalies in the tangent cylinder of the outer core  
94 (Romanowicz et al., 2003), or polar caps with higher concentration of  
95 light elements (Romanowicz and Bréger, 2000).

96

97 Other explanations have invoked the effect of lower mantle structure  
98 where the paths of PKPdf and outer core reference phases PKPbc and  
99 PKPab most diverge. Tkalčić et al. (2002) showed that fitting the SSI-  
100 Alaska anomaly requires rapid lateral variations in the D'' layer.  
101 Recently, Long et al. (2018) proposed a model with a 3% velocity  
102 increase in the lowermost mantle under Alaska, in addition to uniform  
103 inner core anisotropy, to explain the SSI-Alaska anomaly. However, to  
104 explain the entire pattern of travel time and amplitude anomalies with  
105 lower mantle structure alone requires a rather extreme distribution of  
106 heterogeneity near the CMB. Accounting for trade-offs requires either a  
107 thickness up to 650 km with a velocity perturbation of +3%, or P  
108 velocity increases of 9.75% over a thickness of 200 km, which is far in  
109 excess of that seen in tomography: 4 times stronger than that  
110 observed in the regional model of Suzuki *et al.*, (2016) and over 10  
111 times stronger than observed in the global model of Simmons et al.,  
112 (2011). In particular, fitting the variation of the anomaly from the  
113 southwest to the northeast across Alaska requires an increasingly thick  
114 fast D'' layer in the lowermost mantle, in contrast with mineral physics

115 considerations which predict that the D'' discontinuity height decreases  
116 towards the northeast (Sun et al., 2016). Moreover, while PcP-P travel  
117 time measurements do indicate higher than average wavespeeds in  
118 the lower mantle beneath Alaska, the models of Long et al., (2018)  
119 predict PcP-P travel time anomalies 3 times greater than observed  
120 (Ventosa and Romanowicz, 2015). Thus, while models of D''  
121 heterogeneity can explain the SSI-Alaska anomaly, the parameters  
122 required are hard to reconcile with independent observations. On the  
123 other hand, Helffrich and Sacks (1994) suggested that upper mantle  
124 structure could be responsible for some portion of PKP travel time  
125 anomalies. Indeed, in addition to lower mantle heterogeneity, global  
126 tomographic models show strong velocity heterogeneity in the upper  
127 1000 km of the mantle in the vicinity of subduction zones (e.g. Fukao  
128 and Obayashi, 2013), resulting from active tectonic processes near the  
129 surface.

130

131 Here we investigate the source of the SSI-Alaska anomaly, using data  
132 from the USArray deployment in Alaska, which offers high spatial  
133 resolution of PKP travel times. We observe and model the effects of  
134 strong upper mantle structure in our recent 3D upper mantle  
135 tomography model of Alaska (Roecker et al., 2018) on the direction,  
136 slowness and travel time of PKP waves. We show that the complex  
137 upper mantle structure under Alaska is likely responsible for much of

138 the SSI-Alaska anomalous PKPdf observations. Observation and  
139 modelling of similar behaviour in P waves (that do not sample the core)  
140 supports this conclusion.

141

142 **Upper mantle structure beneath Alaska and 3D effects on PKP**  
143 **propagation**

144 Alaska has been subject to multiple episodes of subduction, collision,  
145 and accretion since the mid-Jurassic (Plafker et al., 1994). The present-  
146 day subduction of the Pacific plate along the Aleutian arc began at  
147 ~55Ma (e.g. Scholl et al., 1986) and manifests as steep subduction in  
148 the west, and flat slab subduction in the east, where the Yakutat  
149 terrane, an oceanic plateau with a thick, low-density crust, is currently  
150 being accreted. The structure of Alaska has been extensively studied  
151 using a range of methodologies: receiver functions (e.g. Miller *et al.*,  
152 2018), surface waves (e.g., Feng et al., 2018), arrival time  
153 tomography (e.g. Martin-Short et al., 2016), and joint interpretations of  
154 body and surface waves (e.g. Jiang *et al.*, 2018). These models show  
155 strong and multi-scale velocity heterogeneity throughout the  
156 uppermost 800 km of the mantle.

157

158 The most recent models take advantage of the newly deployed  
159 USArray in Alaska which offers instrumentation with a station spacing  
160 of ~85 km. In a separate study, we obtained a high-resolution model of

161 the upper 400 km of the Alaskan mantle using a joint inversion of  
162 regional and teleseismic P and S travel times from 7 months of data in  
163 2017 (Roecker et al., 2018). The main features of this model are  
164 (Figure 1): a sharply resolved slab of  $\sim 100$  km thickness with  $dV_p \sim$   
165 3%, the Yakutat terrain visible down to 120 km depth with  $dV_p \sim -3\%$ ,  
166 and regions of low velocities on either side of the slab. We note that  
167 the slab structure is both stronger and sharper than in previous models  
168 (Jiang et al., 2018; Martin-Short et al., 2018, 2016).

169

170 Interpretation of PKP travel time anomalies is generally based on the  
171 infinite frequency approximation in a 1D mantle, where seismic waves  
172 are only affected by velocities along the infinitesimal ray path and  
173 where structure only changes with depth. When such corrections for  
174 the tomographically resolved structure are applied, they do not fully  
175 remove scatter in travel times (Bréger et al., 2000). Moreover, it has  
176 been shown that considering the 3D effects of strong velocity  
177 heterogeneity on ray paths improves the fit of tomographic models to  
178 data (Simmons et al., 2012). Finally, when finite frequency effects are  
179 considered, strong heterogeneities, such as a subducting slab, can  
180 affect the travel time, waveform, and frequency content of seismic  
181 waves that intersect it (Helffrich and Sacks, 1994; Vidale, 1987). Of  
182 particular importance for slabs is that the magnitude of the effect is

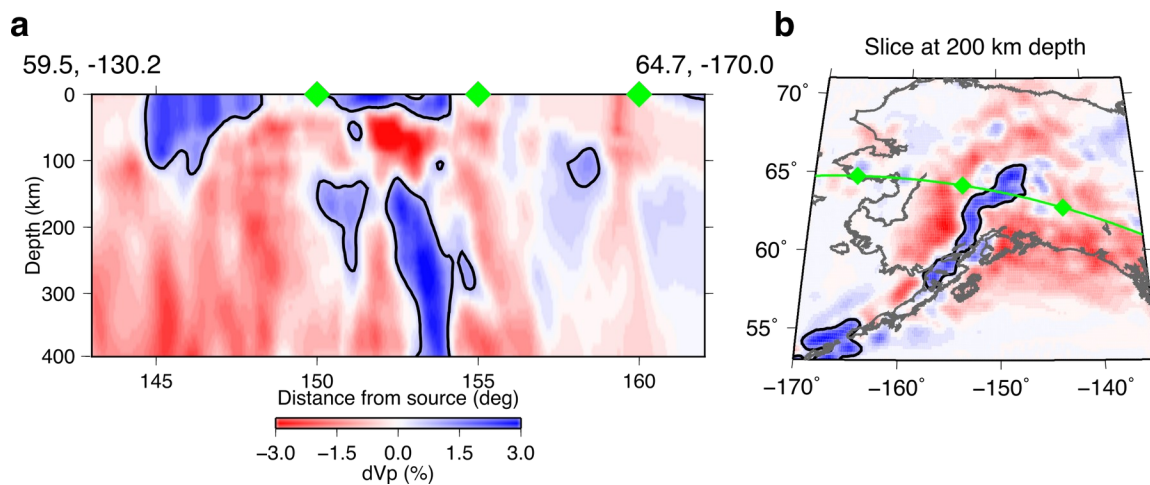


183 strongly dependent on the incident direction of the wave relative to the  
184 dip of the heterogeneity.

185

186 Seismic heterogeneity can distort an incident wave front, leading to  
187 travel time and directional anomalies. Using an array of multiple  
188 stations, the delay time of a wave across the array, or moveout, can be  
189 measured. This moveout is characteristic of the direction from which  
190 the wave arrives in terms of direction on the surface, or back-azimuth  
191 ( $\theta$ ), and the incidence angle, or slowness ( $u$ ). The residual of the travel  
192 time, slowness, and back-azimuth, relative to a 1D reference model,  
193 thus demonstrates the effect that the 3D velocity structure has on the  
194 wavefield (e.g. Durand et al., 2018). Using sub-arrays of the USArray  
195 (e.g. Ventosa and Romanowicz, 2015), now deployed in Alaska, we can  
196 measure the local effects of the structure of the Alaskan mantle.

197



198

199 **Figure 1:** (a) Cross-section of the Vp model of Roecker et al. (2018)  
200 along a representative path from event 6 (Suppl. Table 1) to USArray  
201 stations displayed as per cent deviation from a 1D reference model. (b)  
202 Slice through the model at 200 km depth showing the cross-section  
203 path as the green line. Contour marks 0.8% dVp.

204

## 205 **Methods**

206 We determine the variation of travel time, slowness, and back-azimuth  
207 anomalies across Alaska using a sub-array measurement technique.  
208 We use 6 events in the South Sandwich Islands from 2016 to 2018  
209 (Supplementary table 1) recorded at the USArray and associated  
210 networks in Alaska and Canada (AK, AV, CN, II, IM, IU, TA, and US). We  
211 collect vertical component seismograms, remove the linear trend and  
212 mean from the data, and deconvolve the instrument response. Data  
213 are bandpass filtered between 0.4-2.0 Hz, a range which is found to  
214 best enhance the clarity of PKPdf relative to the noise.

215

216 For each event, we construct sub-arrays of the USArray to measure the  
217 travel time, slowness, and back-azimuth of PKPdf at each location. We  
218 construct a  $1^{\circ} \times 1^{\circ}$  grid across Alaska, and at each grid point we find  
219 the closest station and select an additional 5 to 8 stations around it.  
220 Sub-arrays with fewer than 6 stations in total are excluded, and sub-  
221 arrays with a non-unique station list are not repeated. The minimum

222 number of stations is chosen to ensure high slowness and back-  
 223 azimuth resolution. Meanwhile, the maximum number of stations of 9  
 224 is chosen to minimise the sampling region of each subarray, thus  
 225 increasing spatial resolution between subarrays. At each sub-array we  
 226 window the data 20 s prior to and 40 s after the predicted arrival times  
 227 of PKPdf and PKPab, respectively according to the 1D reference model  
 228 ak135 (Kennett et al., 1995). We set the beampoint to the average  
 229 location of all stations in the subarray. We simultaneously grid search  
 230 over slownesses from 0 to 8 s/deg, and back-azimuths of  $\pm 20^\circ$  relative  
 231 to the great-circle path and construct linear stacks, or vespagrams  
 232 (Davies et al., 1971). We then apply the F-statistic, a coherence  
 233 measure, which effectively suppresses aliasing, thus sharpening  
 234 resolution of slowness and back-azimuth (Frost et al., 2013; Selby,  
 235 2008). The coherence,  $F$ , is computed from the ratio of the sum of the  
 236 energy in the beam,  $b$ , to the summed differences between the beam  
 237 and each trace used to form the beam,  $x_i$ , in a time window,  $M$ ,  
 238 normalized by the number of traces in the beam,  $N$  :

239

$$F = \frac{N-1}{N} \frac{\sum_{t=1}^M b(t)^2}{\sum_{t=1}^M \sum_{i=1}^N (x_i(t) - b(t))^2} \quad (1)$$

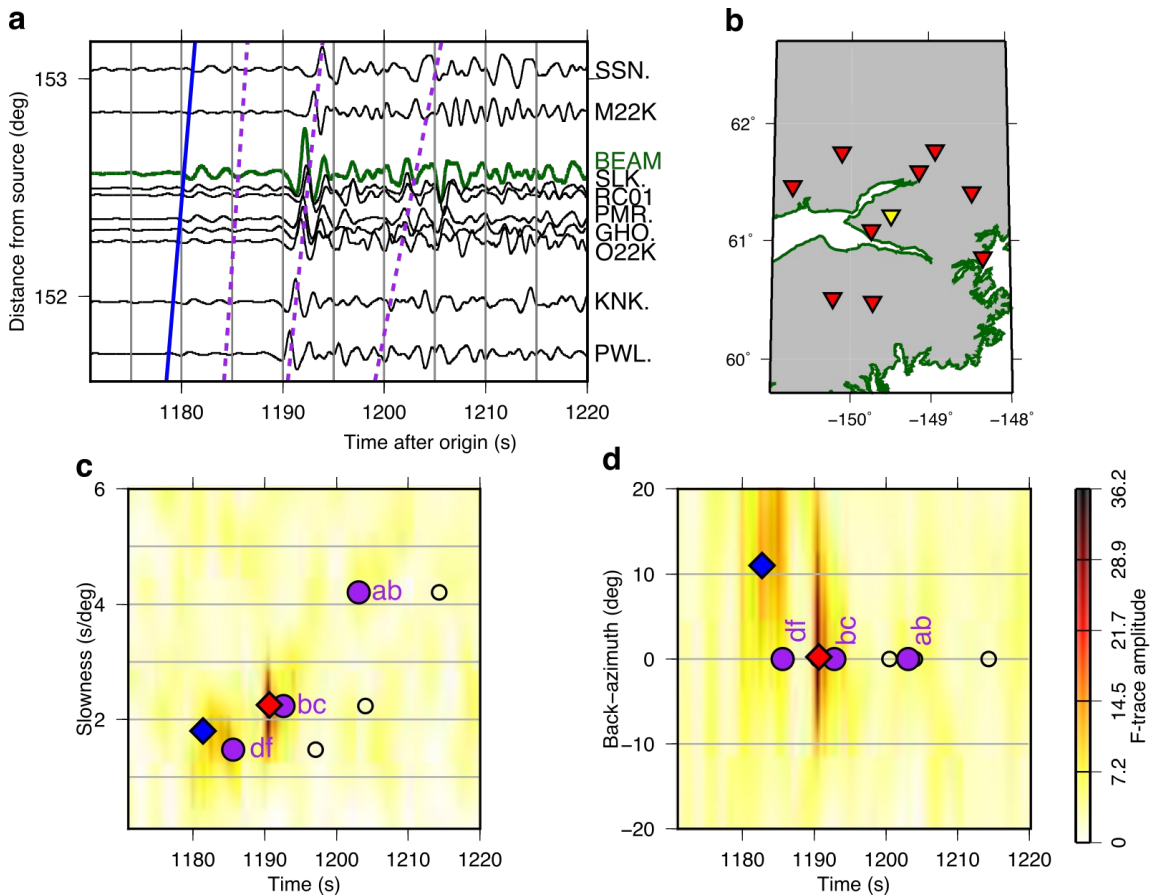
241 We visually inspect the F-vespagrams and select the best fitting  
 242 slowness, back-azimuth, and travel time for PKPdf (Figure 2). We  
 243 display vespagrams calculated for a range of slownesses (Figure 2c)

244 and back-azimuths (Figure 2d) with the other parameter (back-azimuth  
245 and slowness for Figures 2c and 2d, respectively) allowed to vary  
246 depending on the maximum F-value. Thus these 2D time-slowness and  
247 time-back-azimuth vespagrams effectively display a 3D space.  
248 Residual PKPdf travel time and slowness anomalies are measured  
249 relative to predictions from ak135, and travel times are corrected for  
250 ellipticity (Kennett and Gudmundsson, 1996). Back-azimuth residuals  
251 are measured relative to the great-circle path from source to receiver.  
252 Sub-arrays for which PKPdf is absent or not clearly resolved are  
253 discarded. To improve accuracy of the travel time anomaly  
254 measurement, we cross-correlate beams with an empirical PKPdf  
255 wavelet. The wavelet is constructed for each event by adaptively  
256 stacking (Rawlinson and Kennett, 2004) all selected beams from that  
257 event. We then cross correlate each beam with the empirical wavelet  
258 and measure the time shift. To account for errors in origin time and  
259 source location inherent in using PKPdf absolute measurements, we  
260 subtract the median observed travel time from all residual times in the  
261 array (corrections are listed in Supplementary Table 1). We correct  
262 data for a model of inner core anisotropy in the upper 450 km of the  
263 western hemisphere, constructed without using data from the SSI-  
264 Alaska path (model details are given below). This correction accounts  
265 for 1.4 to 2.6 s of travel time anomaly, depending on  $\xi$  and path length

266 in the inner core. A weaker or stronger anisotropy model would remove  
267 less or more of the observed travel time anomaly, respectively.

268

269



270

271 **Figure 2:** Waveform data, station locations, and resultant F-  
272 vepagrams for an example sub-array constructed for event 5 on  
273 2018-08-14 (Suppl. Table 1). (a) PKP wavetrain with PKPdf moveout  
274 marked by the blue line, and 1D predictions for PKPdf, PKPbc, and  
275 PKPab marked by purple broken lines. Individual stations are shown in  
276 black and the filtered beam is shown in green. (b) Map of stations in  
277 the subarray (red) and the beam point (yellow) chosen as the average

278 location of stations in the subarray. F-vespagrams showing time versus  
279 (c) slowness and (d) back-azimuth. PKPdf shows a strong back-azimuth  
280 anomaly, while PKPbc does not, as is predicted by 3D ray-tracing  
281 (Supplementary Figure 2). PKPab appears weak owing to the Hilbert  
282 transform, reducing the amplitude and impulsiveness of the phase. The  
283 picked PKPdf slowness and back-azimuth is shown by the blue  
284 diamond, the maximum F-amplitude, which corresponds to PKPbc, is  
285 shown by the red diamond, and predicted arrivals are shown for the  
286 direct PKP phases (purple circles) and depth phases (open circles).

287

288 The subarray method averages the effects of the structure sampled on  
289 all rays used to form the beam to a single location, the beam point. To  
290 estimate the minimum spatial resolution of our method we calculate  
291 the first Fresnel zone radius for a 1Hz PKP wave at 200 km depth  
292 beneath the surface and add this to the aperture of an example  
293 subarray. We find that the minimum resolution is thus approximately  
294 220 km, or  $2^\circ$ , and thus we cannot interpret structures smaller than  
295 this size, which is about 2 grid points in the regular grids shown in  
296 Figures 3.

297

298 We use synthetic signals to test the resolution of our method. We  
299 simulate signals, combined with real noise at a noise level equivalent  
300 to our data, arriving at an example array from a range of incoming

301 directions. We apply the same vespagram and cross-correlation  
302 approaches as used with the data and determine our time, slowness,  
303 and back-azimuth resolution to be  $\pm 0.1$  s,  $\pm 1^\circ$ , and  $\pm 0.1$  s/deg,  
304 respectively. We test the effect of the number of stations in a subarray  
305 on beam amplitude and find only a 3% difference between the smallest  
306 and largest subarrays. We are thus well able to resolve signals of the  
307 magnitude that we observe.

308

309 We seek to determine the influence of the Alaskan upper mantle on  
310 incoming wave direction and slowness. We forward model PKPdf ray  
311 paths through our regional tomographic model of Alaska using a 3D  
312 ray-tracer derived from the joint inversion approach described in  
313 (Roecker et al., 2010; Comte *et al.*, 2016) and used in the construction  
314 of the 3D model (Roecker et al., 2018). In this approach, we compute  
315 travel times in the 1D model ak135 from the source up to the edges of  
316 the regional tomographic model, and then within the box we apply an  
317 eikonal equation solver in a spherical frame (Zhiwei et al., 2009) to find  
318 the fastest path through the box to the receiver. We calculate PKPdf  
319 travel times through this model and through a simple model, which is  
320 1D throughout. Using the predicted travel times we calculate the  
321 incoming direction of the PKPdf wave at the subarrays used in the  
322 vespagram process. Unlike the vespagram process where we use  
323 waveforms recorded at each station in the subarray, in the ray-tracing

324 process we only have predicted travel times for each station. We select  
325 the same stations used in each subarray and fit a plane to the variation  
326 of travel time as a function of station location in latitude and longitude,  
327 which represents the moveout of the signal. The slope of this surface  
328 can be decomposed into a slowness and a back-azimuth. We calculate  
329 a single travel time for each subarray as the average of the predicted  
330 times for each station. By comparing predictions of the 3D versus the  
331 1D models we compute the travel time ( $dT$ ), slowness ( $du$ ), and back-  
332 azimuth ( $d\theta$ ) anomalies resulting from the 3D upper mantle structure.

333

334 In order to account for the influence of inner core anisotropy on PKPdf  
335 data, we construct a model of inner core western hemisphere  
336 anisotropy ( $167^\circ$  W and  $40^\circ$  E) using the PKPab-df and PKPbc-df  
337 measurements used in Frost and Romanowicz, (2019) and Frost et al.  
338 (*in prep*). To construct a model of inner core anisotropy that can be  
339 used to correct PKPdf travel times on the SSI-Alaska path, but is not  
340 dependent on the SSI-Alaska data, we select only PKPdf data observed  
341 at stations outside of Alaska and with PKPdf paths turning less than  
342 450 km below the ICB (which corresponds to the range of depths  
343 sampled by SSI-Alaska paths). We attribute the entire PKPdf travel time  
344 anomaly to structure in the IC, and convert travel times to velocity

345 anomalies relative to ak135 as:  $\frac{dt}{t} = \frac{-dv}{v}$ , where  $t$  and  $v$  are reference



346 travel times and velocities in the IC, respectively, calculated in model  
347 ak135. This accounts for the difference in path length between the  
348 shallow and more deeply travelling waves. We construct cylindrically  
349 symmetric models of anisotropy, in which the perturbation to an  
350 spherically symmetric model, after Song (1997), is expressed as:

351

$$352 \frac{\delta v}{v_0} = \alpha + \epsilon \cos^2 \xi + \gamma \sin^2 2\xi \quad (2)$$

353

354 where  $v$  and  $\delta v$  represent the reference velocity and velocity  
355 perturbations, respectively, and  $\xi$  the IC paths make with the rotation  
356 axis. By fitting our data with an L1-norm, we determine the coefficients  
357  $\alpha$ ,  $\epsilon$ , and  $\gamma$  to be: -0.028, 2.626, and -0.996, respectively  
358 (Supplementary Figure 1).

359

### 360 **Modelling travel time, slowness and back-azimuth anomalies**

361 After correction for inner core anisotropy as described above, the  
362 observed PKPdf travel time, slowness, and back-azimuth anomalies  
363 show systematic patterns as a function of location across the USArray  
364 (Figure 3). We measure travel time residuals of  $\pm 1.5$  s, slowness  
365 residuals of  $\pm 0.6$  s/deg, and back-azimuth anomalies reaching  $\pm 15$  deg  
366 but more commonly around  $\pm 5$  deg. The patterns are consistent  
367 between events. The most obvious features are:

368 (1) a trend from late to early arrival from the southeast of Alaska,  
369 overlying the Yakutat terrain, towards the northwest

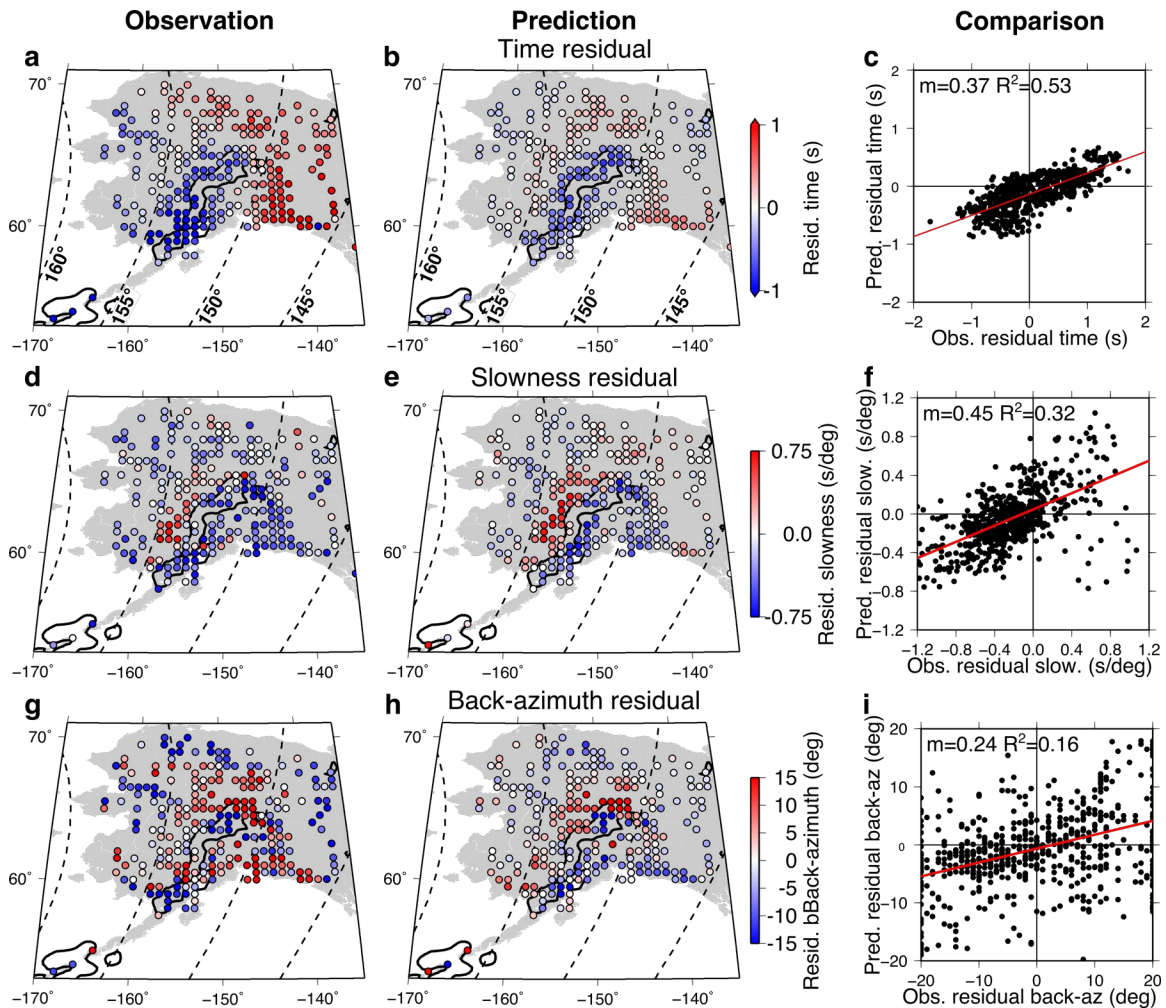
370 (2) low slownesses in the southeast of Alaska, sharply contrasted by a  
371 band of high slownesses trending northeast-southwest across the  
372 middle of Alaska

373 (3) a patch of low back-azimuth residuals in the centre of Alaska,  
374 surrounded by high residuals

375 When viewed in the context of our 3D tomographic model, we find that  
376 these sharp contrasts surround the slab (where the slab is defined by  
377  $>+0.8\%$   $dV_p$ ).

378

379



380

381 **Figure 3:** Observed (left), predicted (middle) and comparison (right) of  
 382 absolute PKPdf ray anomalies from 3D ray-tracing through our  
 383 preliminary tomography model of Alaska, for all 6 events. (a, b and c):  
 384 travel time residuals. (d, e, f): slowness residuals; (g, h, i) back-azimuth  
 385 residuals. The outline of the Alaskan slab at 200 km depth (+0.8%  
 386  $dV_p$ ) from the preliminary tomography model is shown in black. The  
 387 median observed absolute PKPdf travel time is subtracted from each  
 388 event to account for origin time and location errors.

389

390 The corresponding anomalies predicted by 3D ray-tracing through the  
391 upper mantle tomography model of Alaska for all events show a  
392 striking similarity to the observed travel time, slowness, and back-  
393 azimuth anomalies, respectively (Figure 3b, e, and h). The predictions  
394 replicate each of the three main features listed above, most strikingly  
395 the slowness and back-azimuth anomalies. In addition, the model  
396 replicates the trend of increasing and then falling travel time anomaly  
397 with distance for rays on azimuths which intersect the slab  
398 (Supplementary Figure 3), as observed by Romanowicz et al. (2003)  
399 and Long et al. (2018). We see strong agreement of the trends of the  
400 observed and predicted anomalies, but a mismatch in the travel time  
401 anomaly amplitude, with the predicted anomalies being roughly half of  
402 the strength of those observed (Figure 3c, f, and i).

403

404 We also predict travel time, slowness, and back-azimuth anomalies for  
405 PKPab and PKPbc phases. Predicted differential PKPab-df anomalies  
406 range between  $\pm 0.4$  s,  $\pm 0.8$  s/deg, and  $\pm 30$  deg for time, slowness,  
407 and back-azimuths respectively, while differential PKPbc-df anomalies  
408 range between  $\pm 0.1$  s,  $\pm 0.2$  s/deg, and  $\pm 15$  deg for time, slowness,  
409 and back-azimuths respectively. The large variability in back-azimuth  
410 anomalies matches our observations (Figure 2), and likely results from  
411 the greater sensitivity of back-azimuth on a steeply incident phase  
412 (e.g. PKPdf) to small directional changes.

413

414 The degree of qualitative agreement between the observations and  
415 predictions attests to the important influence of upper mantle  
416 heterogeneity on the raypaths and travel times of body waves used to  
417 investigate the inner core. Nonetheless, there are discrepancies, which  
418 point towards limitations: details and strength of the slab model,  
419 unmodelled structure outside of the upper mantle, and potentially the  
420 imprecision of the infinite frequency approximation of ray theory. We  
421 attempt to improve the fit to the observations by perturbing the slab  
422 model and investigate the effect that finite frequency effects may have  
423 by waveform modelling.

424

425 The clearest shortcomings of the model are the magnitude of the  
426 predicted travel time anomalies, which are less than half of those  
427 observed. Tomographic inversions often recover reduced amplitudes of  
428 velocity heterogeneity relative to those resolved by forward waveform  
429 modelling. The velocity anomaly of the slab as recovered in our model  
430 reaches a maximum of around  $\sim 3\%$   $dV_p$ . We test the effect that  
431 stronger heterogeneity may have on the fit by saturating positive  
432 velocity anomalies in the slab regions (which we define as all grid  
433 points with  $dV_p \geq 0.8\%$ ) to 4%. We also test the effect of scaling the  
434 velocity anomalies in the entire model by factors of 2, 2.5, and 3. We  
435 find that the fit between the observed and predicted anomalies

436 improves as we increase the scaling of the tomography model  
437 (Supplementary Figure 4 and Supplementary Table 2). This supports  
438 our hypothesis that some of the misfit between the observed and  
439 predicted times could come from the damping effects of tomographic  
440 models. However, the scatter in the predicted measurements also  
441 increases, which indicates that the details of the slab model should be  
442 improved. Furthermore, the slope of the linear fit between the  
443 observed and predicted slownesses and back-azimuths reaches 1 (thus  
444 is directly proportional) at scaling factors lower than for the travel  
445 times (red text in Suppl. Table 2), thus placing an upper limit on the  
446 travel time anomaly that can come from the upper mantle, since  
447 attempting to match the observed travel time anomalies by scaling  
448 results in over-predicting slowness and back-azimuth anomalies. This  
449 suggests either inaccuracy in modelling the incoming ray direction, or  
450 that matching the observed travel time anomaly requires  
451 heterogeneity outside of the upper mantle. Meanwhile, taking all these  
452 factors into consideration, scaling the tomography model by a factor of  
453 2.5 works best.

454

455 Predicted azimuth anomalies from our tomography model disagree  
456 with the observed back-azimuth in the southeast portion of Alaska. Our  
457 model predicts strong negative back-azimuth anomalies while we  
458 observe strong positive anomalies (Figure 3g,h). However, the model

459 of Martin-Short et al., (2016) better matches the trend of our  
460 observations (Supplementary Figure 5). This discrepancy may arise  
461 from lack of resolution of the Yakutat anomaly in our tomography  
462 model.

463

464 While our model is only resolved down to 400 km depth, previous  
465 tomographic inversions of the Alaskan mantle resolve the slab down to  
466 at least 600 km and potentially beyond, although the high velocity  
467 anomaly of the slab becomes diffuse towards the bottom of the  
468 modelled volume (Martin-Short et al., 2016). Although the model of  
469 Martin-Short et al. (2016) covers a smaller region of Alaska than our  
470 model and shows weaker heterogeneity by a factor of 1.5, this model  
471 images the mantle down to 800 km depth. We use this model to test  
472 the influence of the deeper section of the slab on predicted travel time,  
473 slowness, and back-azimuth anomalies. We compute predicted  
474 anomalies using the whole 800 km of the model, and using the model  
475 cut at 400 km depth to determine the influence of the deeper part of  
476 the slab. We find that fit between the predictions and observations is  
477 marginally improved when calculated using the 800 km thickness of  
478 the model (Supplementary Table 2).

479

480 We compare observations and predictions for different scaling factors  
481 of the tomographic model along cross sections that are representative

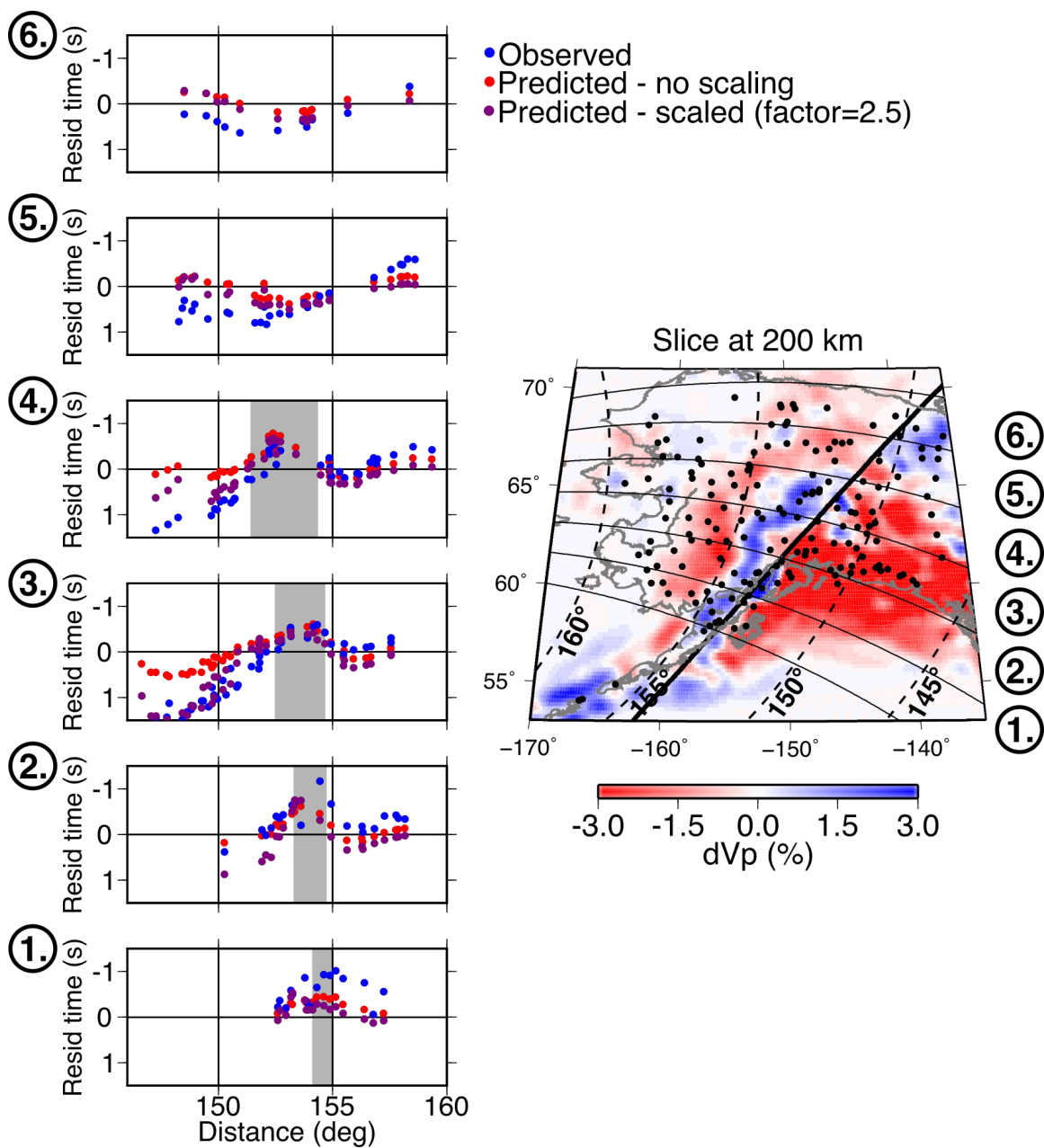
482 of the effects of the Alaskan slab (Supplementary Figure 6). We choose  
483 two slices where we observe both negative travel time residuals over  
484 the slab, and positive travel time residuals either side of the slab.  
485 These azimuth sections (Supplementary Figure 6) allow us to identify  
486 the regional variation of misfit between the observations and  
487 predictions across Alaska, which either point towards local inaccuracies  
488 in the tomography model, or else some other unmodelled structure.  
489 Across all of our events, it appears that the current model of Roecker  
490 et al., (2018) underrepresents the magnitude of the velocity reduction  
491 at shorter distances over the Yakutat (region A in Supplementary  
492 Figure 6); this region is better fit when the model is scaled up by a  
493 factor of 2. In contrast, the predictions of the current model for the  
494 early arrivals caused by the high velocity slab fit the observations  
495 (region B in Supplementary Figure 6) at all azimuths except in the far  
496 southwest towards the Aleutians. The increasingly negative travel time  
497 anomalies at distances  $>157^\circ$  are not fully matched in magnitude by  
498 any of our models, but are best matched by the standard model  
499 (region C in Supplementary Figure 6). Increasing the scaling of the  
500 model appears not to improve the fit to travel time anomalies at  
501 distance  $>157^\circ$ . We produce a hybrid model scaled by a factor of 2.5  
502 before the slab the slab, and 1 over and after the slab. This model  
503 generally fits the data better than any other model (Figure 4), although  
504 it still fails to fully explain the data at distances beyond  $157^\circ$ . This



505 information will inform future iterations of the Alaskan upper mantle  
506 tomography model.

507

508



509

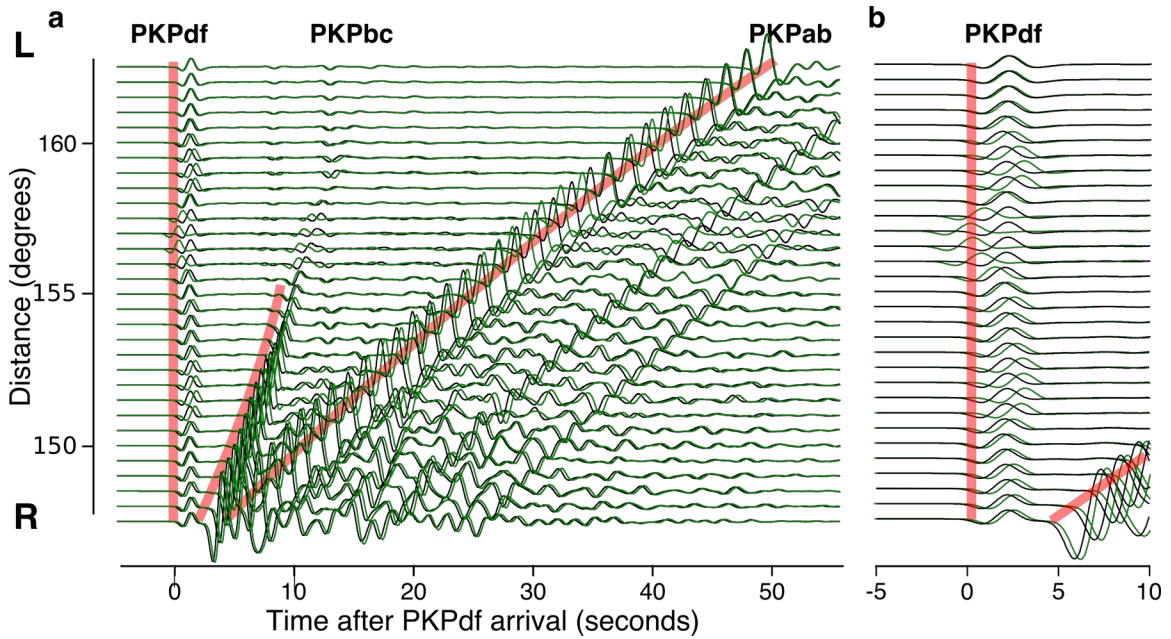
510 **Figure 4:** Left: Absolute PKPdf travel time anomalies as a function of  
511 distance and for different sections through the slab for event 6 on

512 2018-12-11. Observations are shown in blue and predictions from 3D  
513 ray-tracing through the standard and scaled tomography model  
514 (shown on the right) are shown in red and purple, respectively. The  
515 rough location of the slab in each cross section is marked by grey  
516 shading. The tomography model (right) is scaled by a factor of 2.5  
517 before the slab (south-east of the thick black line) and is kept as  
518 standard over and after the slab (north-west of the thick black line).  
519 The model is shown at 200 km depth, with stations shown as black  
520 circles. Azimuths sections shown on the left are labelled on the right.

521

522 In order to estimate the effect of the slab and surrounding  
523 heterogeneity on the travel times and amplitudes of PKPdf, we use  
524 axiSEM (Nissen-Meyer et al., 2014) to simulate the effect of the upper  
525 mantle on the wavefield. We take a 2D slice through the tomography  
526 model (the same as that shown in Figure 1) and calculate waveforms  
527 for a regular station spacing of  $0.5^\circ$  at a maximum frequency of 0.5 Hz.  
528 We find that this results in both positive and negative PKPdf residual  
529 times relative to the 1D prediction of  $\sim 1$ s (Figure 5), which is less than  
530 that observed and predicted by the 3D ray-tracing.

531



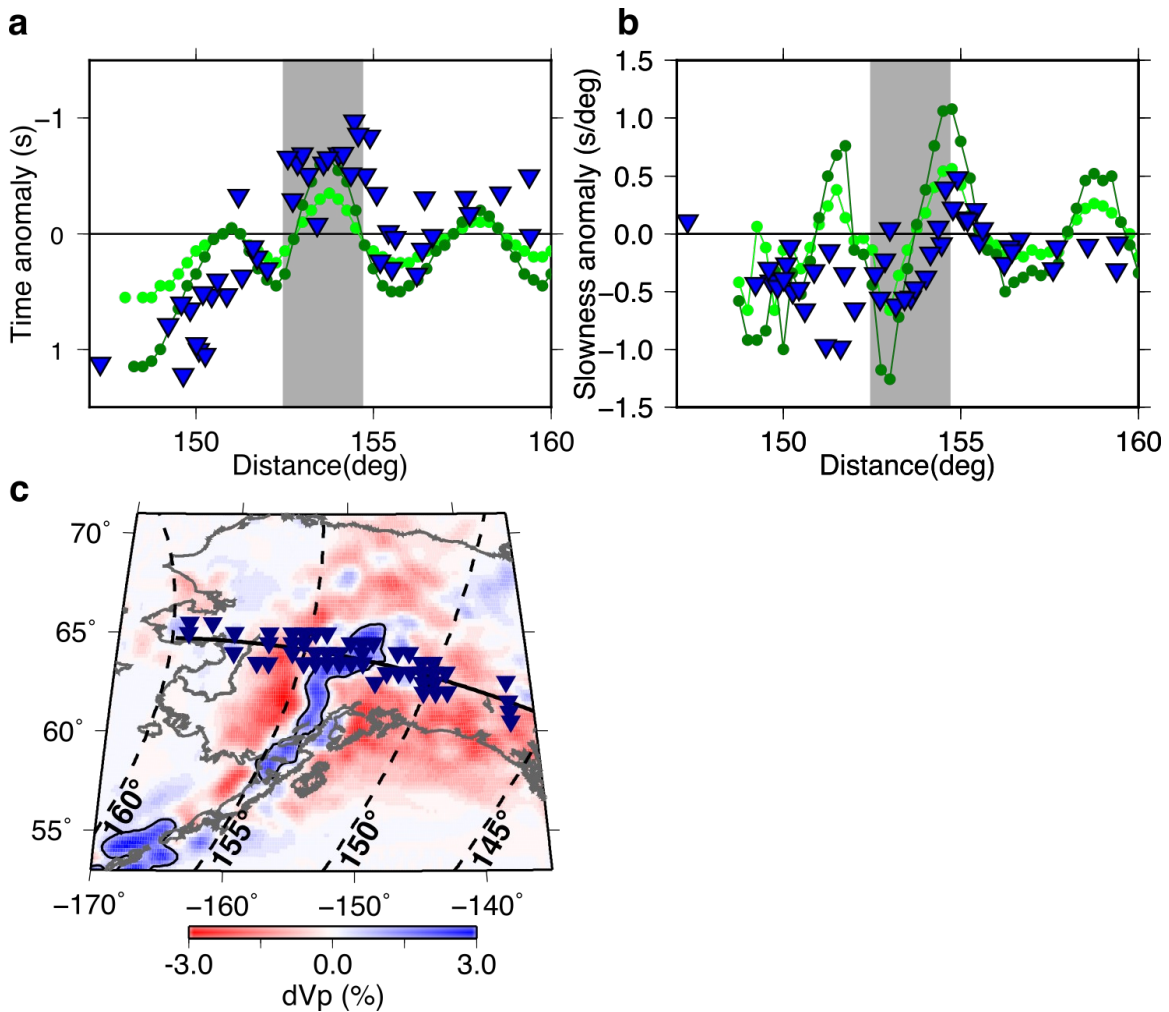
532

533 **Figure 5:** 2.5D synthetic PKP waveforms generated for a 1D model  
 534 (black) and for the cross-section shown in Figure 1 through a saturated  
 535 version of our 3D model (green), aligned on the predicted arrival time  
 536 for PKPdf showing (a) the whole PKP wavetrain, and (b) focussing on  
 537 the PKPdf arrival. The slab model leads to both positive and negative  
 538 travel time delays of the PKP waves and changes in amplitude, relative  
 539 to 1D. Synthetics are calculated at 2s maximum period. Predicted  
 540 arrival times in the 1D model are marked in red.

541

542 To further test the robustness of the observed raypath anomalies, we  
 543 calculate synthetic waveforms through our upper mantle model using a  
 544  $0.04^\circ$  station spacing to allow us to simulate high-resolution arrays. For  
 545 the synthetics, both the subarray spacing and station spacing in each  
 546 subarray are much higher than in our data, but subarray aperture is

547 approximately the same as in the data. We do this to resolve the  
548 effects of the heterogeneity on the waves as accurately as possible but  
549 with a similar spatial sensitivity to the data. This is not designed to  
550 serve as a test of the slowness resolution of our observations. We use  
551 the same vespagram approach as is applied to the data to measure  
552 the slowness anomaly that would result from this upper mantle  
553 heterogeneity. We find similar patterns of both travel time and  
554 slowness anomalies between the synthetics and our observations  
555 (Figure 6). We cannot assess back-azimuth anomalies due to the  
556 rotationally symmetric nature of the synthetic model. As we see in the  
557 3D raytracing results, the observations of slowness are well fit by the  
558 standard model, but the travel times are better fit by a model scaled  
559 by a factor of 2. Some discrepancies may result from the simulations  
560 being run at a maximum period of 2 s for sake of computational cost,  
561 while we make observations on seismograms with a dominant period  
562 of around 1 s.



563

564 **Figure 6:** (a) Travel time and (b) slowness anomalies of PKPdf  
 565 resulting from propagation through the 3D upper mantle model  
 566 relative to a 1D model. The wavefield is simulated using axiSEM  
 567 through a 2.5D slice shown in Figure 1. Displayed are synthetics for the  
 568 standard model (light green), the model scaled by a factor of 2 (dark  
 569 green) and observations (blue inverted triangles) within 1° of the same  
 570 profile for all events. (c) Map of the standard upper mantle tomography  
 571 model at 200 km depth, showing the profile used in the waveform  
 572 simulation in black, with the locations of the selected stations shown as

573 blue triangles. The rough location of the slab in the cross-sections is  
574 shown by grey shading, and by the black contour on the map.

575

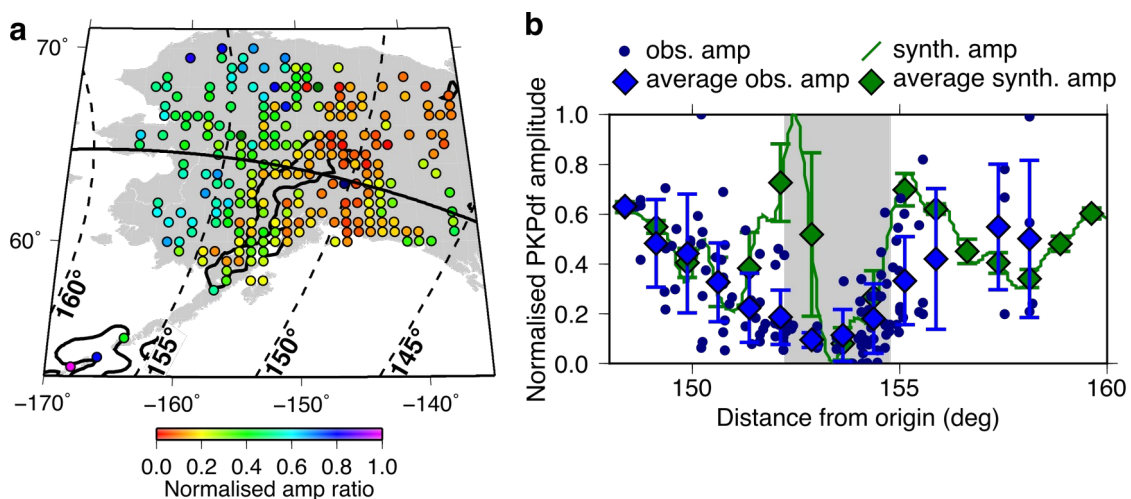
### 576 **Modelling PKPdf amplitude variations**

577 Amplitude variations of the PKPdf wave across Alaska measured  
578 relative to PKPbc were recently reported by Long et al., (2018) and  
579 were attributed to the effects of a high velocity layer in the lowermost  
580 mantle. We measure the PKPdf amplitudes at stations across the  
581 USArray in Alaska relative to the empirical PKPdf wavelet constructed  
582 for each event. We find that PKPdf amplitude decreases over the slab  
583 and that this pattern is consistent between events (Figure 7). The  
584 range of amplitude ratios observed across Alaska is smaller than seen  
585 in amplitude ratios measured on a global scale, which are ascribed to  
586 inner core attenuation (Souriau and Romanowicz, 1997), thus we  
587 suspect a different cause.

588

589 We measure the PKP amplitudes and amplitude ratios predicted by our  
590 waveform models. We find that the trend in the predicted PKPdf  
591 amplitude matches that in the data, except around  $\sim 152^\circ$ , which  
592 corresponds to the edge of the slab (Figure 7). The synthetics predict  
593 larger changes in amplitude over a short distance than is observed.  
594 This likely results from a combination of: (1) the limitations of the  
595 synthetic models, the fact that the calculation is 2.5D and not fully 3D

596 and calculated at only 2 s period and (2) calculating the observed  
 597 amplitude on beams from sub-arrays. The aperture of our sub-arrays is  
 598  $\sim 1^\circ$ , which would smooth out features as sharp as that seen in the  
 599 synthetics. We use moving averages of both the data and the  
 600 synthetics to smooth out the small-scale structure resulting in more  
 601 similar amplitude patterns (diamonds in Figure 7b).  
 602



603  
 604 **Figure 7:** (a) Observed amplitude of PKPdf relative to an empirical  
 605 wavelet, averaged across all 6 events. Amplitudes are normalised to  
 606 the maximum in each event before being combined in the average  
 607 across all events. (b) Observed and synthetic PKPdf amplitudes within  
 608  $\pm 1^\circ$  of section marked by black line, which is the section shown in  
 609 Figure 1. Both observed and synthetic amplitudes are renormalised to  
 610 the same scale. Moving averages and 1 standard deviation error bars  
 611 are calculated every  $1.5^\circ$ . The outline of the Alaskan slab at 200 km

612 depth (+0.8% dVp) from the preliminary tomography model is shown  
613 in black in (a) and by grey shading in (b).

614

## 615 **Discussion**

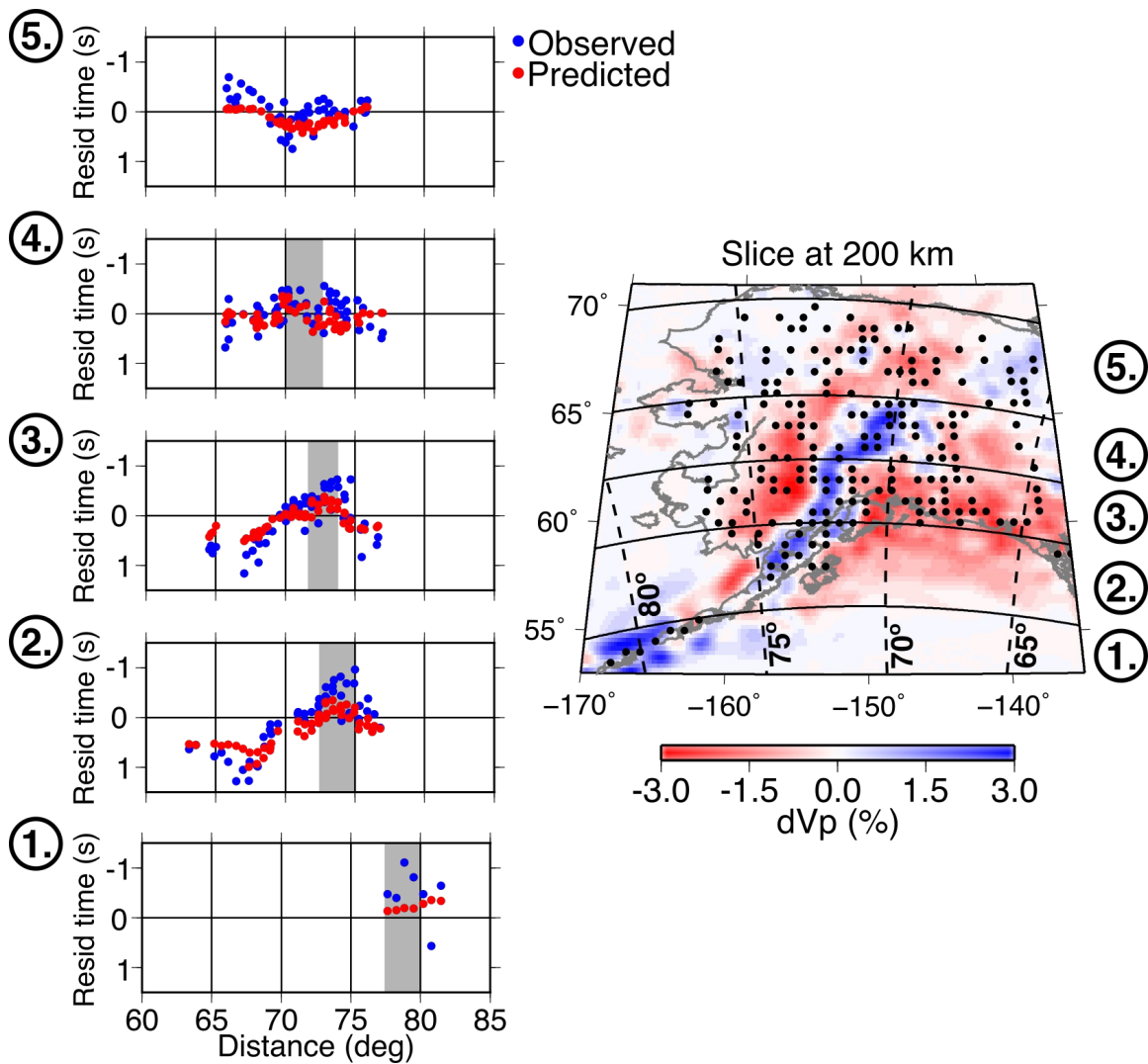
616 In summary, we find that all of our observations of PKPdf travel time,  
617 slowness, back-azimuth, and amplitude variations across Alaska are  
618 consistent with the effects of the slab in the Alaskan upper mantle. In  
619 particular, the subducted slab causes sharp deviations in wave  
620 direction and wave amplitude. Meanwhile, the south-eastern portion of  
621 Alaska shows consistently slow travel times, potentially caused by the  
622 underlying Yakutat lithosphere. These complexities point to the upper  
623 mantle contributing at least 2 s to PKPdf travel time anomalies, which  
624 thus should not be attributed to inner core anisotropy.

625

626 To confirm this slab effect, we measured the travel time, slowness, and  
627 back-azimuth anomalies from three events from the Caribbean and  
628 South America that travel to the USArray in Alaska along similar back-  
629 azimuths as PKP paths from SSI, but at distances corresponding to P  
630 waves (that do not sample the core). Event details are given in  
631 Supplementary Table 3. We applied the same sub-array processing  
632 described here for PKP. While direct P waves arrive at higher  
633 slownesses than PKP, we find very similar patterns to those observed  
634 for PKPdf, and a similarly strong fit between observations and



635 predictions from 3D ray-tracing through an Alaskan tomographic model  
 636 (Supplementary Figure 7). Notably, the observed patterns as a function  
 637 of azimuth and distance are better matched by predicted travel times  
 638 for our unmodified tomographic models than for PKPdf (Figure 8).  
 639 Because P waves sample the slab at shallower depths than PKPdf, this  
 640 indicates that improvement in the deeper part of the slab model may  
 641 be needed, which we will address in a forthcoming study.



642

643 **Figure 8:** Left: Absolute P wave travel time anomalies as a function of  
 644 distance and for different sections through the slab for all three P wave

645 events (Supplementary Table 3), averaged together. Observations  
646 (blue) and predictions (red) from 3D ray-tracing through the standard  
647 tomography model (Roecker et al., 2018). The rough location of the  
648 slab in each cross section is marked by grey shading. To correct for the  
649 different source-receiver distances of these events, we averaged the  
650 observed and predicted P wave times as a function of receiver location,  
651 and then projected the averaged receiver locations relative to the  
652 average P source location. This allows for comparison with the PKPdf  
653 profiles shown in Figure 4 and Supplementary Figure 6. Right: The  
654 tomography model is shown at 200 km depth, with averaged stations  
655 shown as black circles. Azimuths sections shown on the left are  
656 labelled on the right.

657

658 Upper mantle structure in other regions, such as the Scotia slab under  
659 the South Sandwich Islands source region (Fukao et al., 2001), may  
660 also influence the observed anomalies, yet is not modelled here.  
661 Measurements of PcP-P differential travel times in the region around  
662 the Scotia slab show a large range of travel time anomalies (Tkalčić,  
663 2010). The range of these anomalies is of a similar magnitude to PKPdf  
664 travel time anomalies observed in Alaska from the same source region,  
665 but unlike for PKPdf, they are scattered and show no systematic  
666 variation. Furthermore, Romanowicz et al. (2003) demonstrated that  
667 the patterns of PKP residual travel time with  $\xi$ , distance, and azimuth  
668 recorded in Alaska were observed for all SSI events, regardless of  
669 location. Long et al. (2018) observe that the location of the SSI event  
670 does change the distance (relative to the event) at which the trend of

671 increasing  $dT$  is observed, but we find that the geographic location of  
672 the trend is the same for all events: over the Alaskan slab. Thus, while  
673 mantle structure near the Scotia slab may contribute to the  
674 observations in terms of additional scatter, it is unlikely to be the  
675 cause of the systematic pattern of PKPdf anomalies observed in Alaska.  
676 Moreover, the range of source locations and depths used in this study  
677 would likely reduce any systematic bias in our observations that would  
678 result from the Scotia slab.

679

680 The travel time of PKPdf is known to be affected by anisotropy in the  
681 inner core (Supplementary Figure 1), thus we add a correction to the  
682 observed travel times. The model of inner core anisotropy used is  
683 derived from data sampling the same depth range and in the same  
684 hemisphere of the inner core as the South Sandwich Islands to Alaska  
685 data. The strength of this correction affects the travel time anomaly  
686 that we ultimately attribute to the upper mantle. Since the travel time  
687 anomaly from the inner core does depend on station location this does  
688 affect the moveout of the PKPdf wave across each sub array, but the  
689 effect is negligible given the small size of the sub arrays. However, the  
690 correction significantly improves the match between the observed and  
691 predicted travel time anomalies (Supplementary Figure 8).

692

693 As recently suggested by Long et al. (2018) and mentioned earlier,  
694 lower mantle heterogeneity could influence PKP travel time anomalies.  
695 However, we calculate that the magnitude of lower mantle  
696 heterogeneity that would also be compatible with other observations of  
697 D'' structure, in particular PcP-P travel times (Ventosa and  
698 Romanowicz, 2015), would contribute travel time anomalies on the  
699 order of no more than  $\sim 1$ s. Core-Mantle Boundary structure instead  
700 might contribute to measurement scatter or the event-specific shift  
701 from the predicted times (listed in last column of Supplementary Table  
702 1). Alternatively, the event-specific shift may result from source  
703 location and origin time errors. Moreover, our upper mantle model  
704 reproduces the pattern of travel time anomalies with distance from the  
705 events in the South Sandwich Islands (Supplementary Figure 4). The fit  
706 is more satisfactory than that achieved by Long et al. (2018) using  
707 lower mantle heterogeneity, and is also capable of explaining the  
708 change in pattern with back-azimuth (Supplementary Figure 3).  
709 Furthermore, the upper mantle model is capable of reproducing the  
710 patterns of slowness and back-azimuth anomalies. Contamination of  
711 PKP waves by upper mantle heterogeneity thus provides a single, self-  
712 contained explanation for patterns previously attributed to the lower  
713 mantle, outer core, and or inner core.

714

715 **Conclusion**

716 We find that the pattern of slowness, back-azimuth, and travel time  
717 anomalies measured for PKPdf at sub-arrays of the USArray in Alaska  
718 match the patterns predicted by a high-resolution model of the Alaskan  
719 upper mantle. The strong similarity of the observed slowness and back-  
720 azimuths to those predicted using only upper mantle heterogeneity  
721 suggests that it is the main source of the anomalies. This is also  
722 confirmed by analysis of direct P waves along azimuths similar to the  
723 SSI to Alaska PKP paths considered here. While other structure in the  
724 lower mantle and upper mantle on the source side may also contribute  
725 to the observed scatter in travel time residuals, we conclude that the  
726 dominant cause of the SSI-Alaskan anomaly is the Alaskan subduction  
727 zone. As such, this motivates further improvements in characterizing  
728 the structure of the Alaska slab and its surroundings. More generally,  
729 care must be taken when interpreting travel time anomalies from  
730 regions with strong upper mantle structure in terms of inner core  
731 structure.

732

### 733 **Acknowledgements**

734 We thank the International Seismological Centre (ISC) for access to the  
735 EHB and On-line Bulletins, <http://www.isc.ac.uk>, Internatl. Seismol.  
736 Cent., Thatcham, United Kingdom, 2015. The facilities of IRIS Data  
737 Services, and specifically the IRIS Data Management Center, were used  
738 for access to waveforms, related metadata, and/or derived products

739 used in this study. IRIS Data Services are funded through the  
740 Seismological Facilities for the Advancement of Geoscience and  
741 EarthScope (SAGE) Proposal of the National Science Foundation under  
742 Cooperative Agreement EAR-1261681. Waveform simulations were  
743 performed using The Extreme Science and Engineering Discovery  
744 Environment (XSEDE) supported by grants TG-EAR180020 and TG-  
745 EAR170001. This work was supported by EAR-1135452 and NSF grant  
746 EAR-1829283.

747

#### 748 **References**

- 749 Bréger, L., Tkalčić, H., Romanowicz, B.A., 2000. The effect of D'' on  
750 PKP(AB-DF) travel time residuals and possible implications for inner  
751 core structure. *Earth Planet. Sci. Lett.* 175, 133-143.  
752 [https://doi.org/10.1016/S0012-821X\(99\)00286-1](https://doi.org/10.1016/S0012-821X(99)00286-1)
- 753 Cao, A., Romanowicz, B., 2007. Test of the innermost inner core  
754 models using broadband PKIKP travel time residuals. *Geophys. Res.*  
755 *Lett.* 34, 1-5. <https://doi.org/10.1029/2007GL029384>
- 756 Comte, D., Carrizo, D., Roecker, S., Ortega-Culaciati, F., Peyrat, S.,  
757 2016. Three-dimensional elastic wave speeds in the northern Chile  
758 subduction zone: Variations in hydration in the supraslab mantle.  
759 *Geophys. J. Int.* 207, 1080-1105.  
760 <https://doi.org/10.1093/gji/ggw318>
- 761 Creager, K.C., 1999. Large-scale variations in inner core anisotropy. *J.*

762 Geophys. Res. 104, 23127–23139.  
763 <https://doi.org/10.1029/1999jb900162>

764 Davies, D., Kelly, E.J., Filson, J.R., 1971. Vespa Process for Analysis of  
765 Seismic Signals. Nat. Phys. Sci. 232, 8–13.  
766 <https://doi.org/10.1038/physci232008a0>

767 Durand, S., Thomas, C., Jackson, J.M., 2018. Constraints on D" beneath  
768 the North Atlantic region from P and S traveltimes and amplitudes.  
769 Geophys. J. Int. 216, 1132–1144. <https://doi.org/10.1093/gji/ggy476>

770 Frost, D.A., Romanowicz, B., 2019. On the orientation of the fast and  
771 slow directions of anisotropy in the deep inner core. Phys. Earth  
772 Planet. Inter. 286, 101–110.  
773 <https://doi.org/10.1016/j.pepi.2018.11.006>

774 Frost, D.A., Romanowicz, B., 2017. Constraints on Inner Core  
775 Anisotropy Using Array Observations of P'P'. Geophys. Res. Lett.  
776 44, 10,878–10,886. <https://doi.org/10.1002/2017GL075049>

777 Frost, D.A., Rost, S., Selby, N.D., Stuart, G.W., 2013. Detection of a tall  
778 ridge at the core-mantle boundary from scattered PKP energy.  
779 Geophys. J. Int. 195. <https://doi.org/10.1093/gji/ggt242>

780 Fukao, Y., Obayashi, M., 2013. Subducted slabs stagnant above,  
781 penetrating through, and trapped below the 660 km discontinuity.  
782 J. Geophys. Res. 118, 5920–5938.  
783 <https://doi.org/10.1002/2013JB010466>

784 Fukao, Y., Widiyantoro, S., Obayashi, M., 2001. Stagnant slabs in the

785 upper and lower mantle transition region 291–323.

786 Garcia, R., Tkalčić, H., Chevrot, S., 2006. A new global PKP data set to  
787 study Earth's core and deep mantle. *Phys. Earth planet. Int.* 159,  
788 15–31. <https://doi.org/10.1016/j.pepi.2006.05.003>

789 Helffrich, G., Sacks, S., 1994. Scatter and bias in differential PKP travel  
790 times and implications for mantle and core phenomena. *Geophys.*  
791 *Res. Lett.* 21, 2167–2170. <https://doi.org/10.1029/94GL01876>

792 Irving, J.C.E., Deuss, A., 2011. Hemispherical structure in inner core  
793 velocity anisotropy. *J. Geophys. Res.* 116, 1–17.  
794 <https://doi.org/10.1029/2010JB007942>

795 Ishii, M., Dziewonski, A.M., 2002. The innermost inner core of the earth:  
796 Evidence for a change in anisotropic behavior at the radius of  
797 about 300 km. *Proc. Nat. Acad. Sci. USA* 99, 14026–14030. <https://doi.org/10.1073/pnas.172508499>

798

799 Jiang, C., Schmandt, B., Ward, K.M., Lin, F.C., Worthington, L.L., 2018.  
800 Upper Mantle Seismic Structure of Alaska From Rayleigh and S  
801 Wave Tomography. *Geophys. Res. Lett.* 45, 10,350–10,359. <https://doi.org/10.1029/2018GL079406>

802

803 Kennett, B.L.N., Engdahl, E.R., Buland, R., 1995. Constraints on seismic  
804 velocities in the Earth from traveltimes. *Geophys. J. Int.* 122, 108–  
805 124. <https://doi.org/10.1111/j.1365-246X.1995.tb03540.x>

806 Kennett, B.L.N., Gudmundsson, O., 1996. Ellipticity corrections for  
807 seismic phases. *Geophys. J. Int.* 127, 40–48.



808 <https://doi.org/10.1111/j.1365-246X.1996.tb01533.x>

809 Leykam, D., Tkalčić, H., Reading, A.M., 2010. Core structure re-  
810 examined using new teleseismic data recorded in Antarctica:  
811 Evidence for, at most, weak cylindrical seismic anisotropy in the  
812 inner core. *Geophys. J. Int.* 180, 1329–1343.  
813 <https://doi.org/10.1111/j.1365-246X.2010.04488.x>

814 Li, X., Cormier, V.F., 2002. Frequency-dependent seismic attenuation in  
815 the inner core, 1. A viscoelastic interpretation. *J. Geophys. Res.*  
816 107, ESE 13-1-ESE 13-20. <https://doi.org/10.1029/2002JB001795>

817 Long, X., Kawakatsu, H., Takeuchi, N., 2018. A Sharp Structural  
818 Boundary in Lowermost Mantle Beneath Alaska Detected by Core  
819 Phase Differential Travel Times for the Anomalous South Sandwich  
820 Islands to Alaska Path. *Geophys. Res. Lett.* 45, 176–184.  
821 <https://doi.org/10.1002/2017GL075685>

822 Lythgoe, K.H., Deuss, A., Rudge, J.F., Neufeld, J.A., 2014. Earth's inner  
823 core: Innermost inner core or hemispherical variations? *Earth*  
824 *Planet. Sci. Lett.* 385, 181–189.  
825 <https://doi.org/10.1016/j.epsl.2013.10.049>

826 Martin-Short, R., Allen, R., Bastow, I.D., Porritt, R.W., Miller, M.S., 2018.  
827 Seismic Imaging of the Alaska Subduction Zone: Implications for  
828 Slab Geometry and Volcanism. *Geochem. Geophys. Geosyst.* 19,  
829 4541–4560. <https://doi.org/10.1029/2018GC007962>

830 Martin-Short, R., Allen, R.M., Bastow, I.D., 2016. Subduction geometry

831 beneath south central Alaska and its relationship to volcanism.  
832 Geophys. Res. Lett. 43, 9509–9517.  
833 <https://doi.org/10.1002/2016GL070580>

834 Miller, M.S., O’Driscoll, L.J., Porritt, R.W., Roeske, S.M., 2018. Multiscale  
835 crustal architecture of Alaska inferred from P receiver functions.  
836 Lithosphere 267–278. <https://doi.org/10.1130/l701.1>

837 Morelli, A., Dziewonski, A.M., Woodhouse, J.H., 1986. Anisotropy of the  
838 inner core inferred from PKIKP travel times. Geophys. Res. Lett. 13,  
839 1545–1548. <https://doi.org/10.1029/GL013i013p01545>

840 Nissen-Meyer, T., Van Driel, M., Stähler, S.C., Hosseini, K., Hempel, S.,  
841 Auer, L., Colombi, A., Fournier, A., 2014. AxiSEM: Broadband 3-D  
842 seismic wavefields in axisymmetric media. Solid Earth 5, 425–445.  
843 <https://doi.org/10.5194/se-5-425-2014>

844 Plafker, G., Moore, J.C., Winkler, G.R., 1994. Geology of the southern  
845 Alaska margin, The Geology of Alaska.  
846 <https://doi.org/10.1130/dnag-gna-g1.389>

847 Rawlinson, N., Kennett, B.L.N., 2004. Rapid estimation of relative and  
848 absolute delay times across a network by adaptive stacking.  
849 Geophys. J. Int. 157, 332–340. [https://doi.org/10.1111/j.1365-](https://doi.org/10.1111/j.1365-246X.2004.02188.x)  
850 [246X.2004.02188.x](https://doi.org/10.1111/j.1365-246X.2004.02188.x)

851 Roecker, S., Baker, B., McLaughlin, J., 2010. A finite-difference  
852 algorithm for full waveform teleseismic tomography. Geophys. J.  
853 Int. 181, 1017–1040. <https://doi.org/10.1111/j.1365->

854 246X.2010.04553.x

855 Roecker, S. W., D. A. Frost, and B. A Romanowicz, Structure of the  
856 Crust and Upper Mantle beneath Alaska Determined from the Joint  
857 Inversion of Arrival Times and Waveforms of Regional and  
858 Teleseismic Body Waves, American Geophysical Union, Fall  
859 Meeting 2018, abstract #S31C-0518.

860 Romanowicz, B., Bréger, L., 2000. Anomalous splitting of free  
861 oscillations: A reevaluation of possible interpretations. *J. Geophys.*  
862 *Res.* 105, 21559–21578. <https://doi.org/10.1029/2000jb900144>

863 Romanowicz, B., Cao, A., Godwal, B., Wenk, R., Ventosa, S., Jeanloz, R.,  
864 2015. Seismic anisotropy in the Earth's innermost inner core:  
865 testing structural models against mineral physics predictions.  
866 *Geophys. Res. Lett.* 93–100. <https://doi.org/10.1002/2015GL066734>

867 Romanowicz, B., Tkalčić, H., Bréger, L., 2003. On the Origin of  
868 Complexity in PKP Travel Time Data. *Earth's Core Dyn. Struct.*  
869 *Rotat.* 31–44. <https://doi.org/10.1029/GD031p0031>

870 Scholl, D.W., Vallier, T.L., Stevenson, A.J., 1986. Terrane accretion,  
871 production, and continental growth: a perspective based on the  
872 origin and tectonic fate of the Aleutian- Bering Sea region. *Geology*  
873 14, 43–47. [https://doi.org/10.1130/0091-](https://doi.org/10.1130/0091-7613(1986)14<43:TAPACG>2.0.CO;2)  
874 [7613\(1986\)14<43:TAPACG>2.0.CO;2](https://doi.org/10.1130/0091-7613(1986)14<43:TAPACG>2.0.CO;2)

875 Selby, N.D., 2008. Application of a generalized F detector at a  
876 seismometer array. *Bull. Seism. Soc. Am.* 98, 2469–2481.

877 <https://doi.org/10.1785/0120070282>

878 Shearer, P.M., 1994. Constraints on inner core anisotropy from PKP(DF)  
879 travel times. *J. Geophys. Res. Solid Earth* 99, 19647–19659. [https://](https://doi.org/10.1029/94jb01470)  
880 [doi.org/10.1029/94jb01470](https://doi.org/10.1029/94jb01470)

881 Simmons, N.A., Myers, S.C., Johannesson, G., 2011. Global-scale P  
882 wave tomography optimized for prediction of teleseismic and  
883 regional travel times for Middle East events: 2. Tomographic  
884 inversion. *J. Geophys. Res.* 116, 1–31.  
885 <https://doi.org/10.1029/2010JB007969>

886 Simmons, N.A., Myers, S.C., Johannesson, G., Matzel, E., 2012. LLNL-  
887 G3Dv3: Global P wave tomography model for improved regional  
888 and teleseismic travel time prediction. *J. Geophys. Res.* 117.  
889 <https://doi.org/10.1029/2012JB009525>

890 Song, X., 1997. Anisotropy of the Earth's inner core. *Rev. Geophys.*  
891 297–313. <https://doi.org/10.1029/93JB0340310.1029/9>

892 Souriau, A., Romanowicz, B., 1997. Anisotropy in the inner core:  
893 Relation between P-velocity and attenuation. *Phys. Earth planet.*  
894 *Int.* 101, 33–47. [https://doi.org/10.1016/S0031-9201\(96\)03242-6](https://doi.org/10.1016/S0031-9201(96)03242-6)

895 Stixrude, L., Cohen, R.E., 1995. High-Pressure Elasticity of Iron and  
896 Anisotropy of Earth's Inner Core. *Science* (80-. ). 267, 1972–1975.

897 Su, W., Dziewonski, A.M., 1995. Inner core anisotropy in three  
898 dimensions. *J. Geophys. Res.* 100, 9831–9852.  
899 <https://doi.org/10.1029/95JB00746>

900 Sun, D., Helmberger, D., Miller, M.S., Jackson, J.M., 2016. Major  
901 disruption of D'' beneath Alaska. *J. Geophys. Res.* 121, 3534–3556.  
902 <https://doi.org/10.1002/2015JB012534>

903 Suzuki, Y., Kawai, K., Geller, R.J., Borgeaud, A.F.E., Konishi, K., 2016.  
904 Waveform inversion for 3-D S-velocity structure of D'' beneath the  
905 Northern Pacific: Possible evidence for a remnant slab and a  
906 passive plume dr. *Earth, Planets Sp.* 68.  
907 <https://doi.org/10.1186/s40623-016-0576-0>

908 Tanaka, S., Hamaguchi, H., 1997. Degree one heterogeneity and  
909 hemispherical variation of anisotropy in the inner core from  
910 PKP(BC)-PKP(DF) times. *J. Geophys. Res.* 102, 2925–2938.  
911 <https://doi.org/10.1029/96JB03187>

912 Tkalčić, H., 2010. Large variations in travel times of mantle-sensitive  
913 seismic waves from the South Sandwich Islands: Is the Earth's  
914 inner core a conglomerate of anisotropic domains? *Geophys. Res.*  
915 *Lett.* 37, 1–6. <https://doi.org/10.1029/2010GL043841>

916 Tkalčić, H., Romanowicz, B., Houy, N., 2002. Constraints on D''  
917 structure using PKP (AB-DF), PKP (BC-DF) and PcP-P traveltimes  
918 data from broad-band records. *Geophys. J. Int.* 148, 599–616.  
919 <https://doi.org/10.1046/j.1365-246X.2002.01603.x>

920 Tkalčić, H., Young, M., Muir, J.B., Davies, D.R., Mattesini, M., 2015.  
921 Strong, Multi-Scale Heterogeneity in Earth's Lowermost Mantle. *Sci.*  
922 *Rep.* 5, 1–8. <https://doi.org/10.1038/srep18416>

923 Ventosa, S., Romanowicz, B., 2015. Extraction of weak PcP phases  
924 using the slant-stacklet transform - II: constraints on lateral  
925 variations of structure near the core-mantle boundary. *Geophys. J.*  
926 *Int.* 203, 1227-1245. <https://doi.org/10.1093/gji/ggv364>

927 Vidale, J.E., 1987. Waveform effects of a high-velocity, subducted slab.  
928 *Geophys. Res. Lett.* 14, 542-545.  
929 <https://doi.org/10.1029/GL014i005p00542>

930 Vinnik, L., Romanowicz, B., Bréger, L., 1994. Anisotropy in the center of  
931 the inner core. *Geophys. Res. Lett.* 21, 1671-1674.  
932 <https://doi.org/10.1029/94GL01600>

933 Woodhouse, J.H., Giardini, D., Li, X. -D, 1986. Evidence for inner core  
934 anisotropy from free oscillations. *Geophys. Res. Lett.* 13, 1549-  
935 1552. <https://doi.org/10.1029/GL013i013p01549>

936 Zhiwei, L., Roecker, S., Zhihai, L., Bin, W., Haitao, W., Schelochkov, G.,  
937 Bragin, V., 2009. Tomographic image of the crust and upper  
938 mantle beneath the western Tien Shan from the MANAS broadband  
939 deployment: Possible evidence for lithospheric delamination.  
940 *Tectonophysics* 477, 49-57.  
941 <https://doi.org/10.1016/j.tecto.2009.05.007>

942